J Mater Sci: Mater Electron (2021) 32:24296–24307

Sb–doped ZnO ceramics: NTC thermistors with high temperature sensitivity and electrical stability

Bicai Li[1,2], Zhicheng Li[1], Dicheng Peng[1], Linling Huang[1], Shuyan Zhang[1], and
Hong Zhang[1,*]

[1] School of Materials Science and Engineering, Central South University, Chang Sha 410083, China
[2] School of Materials and Chemical Engineering, Hunan City University, Yi Yang 413000, China

Received: 4 July 2021
Accepted: 23 August 2021

ABSTRACT

Sb-modified ZnO ceramics ($Zn_{1-x}Sb_xO$, $x = 0$, 0.001, 0.003, 0.005, 0.007, 0.010, 0.015, 0.020, 0.025) were prepared by the conventional solid-state reaction process. The phase component, electrical properties and electrical stabilities were investigated. $Zn_{1-x}Sb_xO$ ceramics have hexagonal wurtzite structure and show typical characteristics of negative temperature coefficient of resistivity. The room temperature resistivity and temperature sensitivity can be adjusted by Sb element doping. For various contents of Sb-ions, the prepared ceramics have temperature sensitivity of $B_{25/85}$ values from 2284 to 4754 K. After aging treatment at 150 °C, the ceramics have resistance change rates ($\Delta R/R_0$) ranging from 1.44 to 2.17%. The aging induced change of resistance mainly resulted from the grain effect. The aging characteristics were discussed with the complex impedance spectra of ceramics and the variation of valent states of Sb-ions before and after aging.

1 Introduction

A negative temperature coefficient (NTC) thermistor has the characteristic that its resistance decreases with the increasing of temperature. NTC thermistors are widely used in temperature detection and compensation, surge suppression, temperature control, etc. [1–4]. The traditional NTC thermistors are normally made of transition metal oxides with AB_2O_4 type spinel structure, in which spinel manganates are the typical system such as $Co_{0.98}Mn_{2.02}O_4$, $NiMn_2O_4$, $NiMn_{2-x}Zr_xO_4$ and $Ni_{0.75}Mn_{(2.25-x-y)}Cr_xFe_yO_4$ [5–9]. The polaron hopping model is generally considered to be the main conduction mechanism in the traditional NTC thermistors, *i.e.*, charge carriers jump between the octahedral B-site cations such as Mn^{3+} and Mn^{4+} ions in spinel manganate [10–13]. ABO_3 type perovskite NTC thermistors such as $LaCrO_3$, $LaMnO_3$, $YFeO_3$ and $BaTiO_3$, etc. are another concerned system [14–17]. In the meanwhile, some semiconductors with single cationic oxides such as SnO_2, CuO, NiO and ZnO have also been studied for the applications for NTC thermistors in recent years [16, 18–20]. Those single cationic oxides have unique merit for that their NTC temperature sensitivity (B value) and room temperature resistivity (ρ_{25}) can

---

Address correspondence to E-mail: hzhang@csu.edu.cn

https://doi.org/10.1007/s10854-021-06896-1

be adjusted effectively with different type and quantity of doping elements. For example, the work by Yang et al. showed that ρ_{25} from 47.94 to 1.024 MΩ·cm and $B_{25/85}$ values from 2582 to 8019 K were achieved in NiO-based thermistors by changing the dopant concentrations of B^{3+}- and Na^{+}- ions [12]. The $B_{25/85}$ values ranged from 641 to 5085 K and ρ_{25} ranged from 4.77 to 48.9 MΩ·cm of Sb–doped SnO_2 ceramics modified by Zr-ions were reported by Ouyang et al. [21].

In the meanwhile, electrical stability is another key property for practical application of NTC thermistors. The electrical stability for NTC thermistors is often characterized by the resistance drift rate ($\Delta R/R_0$) after being serviced for a period of time at a certain temperature, which is usually selected at 125 °C or 150 °C in air for the ordinary temperature NTC thermistors. Some researchers have reported the electrical stability of traditional spinel and perovskite thermistors [4, 15, 22–24]. Fang et al. investigated the aging behavior of nickel manganite NTC ceramics and pointed out the aging mechanism basing on model of cationic vacancy-assisted cation [23]. Recently, Gao et al. used an oxygen adsorption dissociation model to explain the aging stability of Bi-modified $(Zn_{0.4}Ni_{0.6})_{1-x}Na_xO$ ceramics [25].

As a non-toxic and low-cost semiconductor oxide, ZnO has attracted extensive attention due to its potential applications in luminescence, piezoelectric, semiconductor, photocatalytic materials and varistor [26–30]. NTC ceramics based on Al/La/Cu modified ZnO was reported by Li et al. and showed adjustable ρ_{25} (0.65 ~ 3280 kΩ·cm) and $B_{25/85}$ values (2500 ~ 5850 K) as well as high electrical stability with $\Delta R/R_0$ less than 2% [20]. This indicated that ZnO based ceramics are a new system of potential NTC thermistors. In the work by Li et al. [20], three kinds of cations were used to adjust the electrical properties of ZnO based NTC thermistors. It should be interesting that the electrical properties of ZnO based NTC thermistor could be adjusted with only single cation doping. In this work, single element Sb doped ZnO ceramics were prepared without additional sintering aids. The results show that Sb-doped ZnO ceramics show typical NTC effect with high *B* values and high electrical stability.

2 Experimental

2.1 Material preparation

Sb–doped ZnO ceramics with nominal formula of $Zn_{1-x}Sb_xO$ (x = 0, 0.001, 0.003, 0.005, 0.007, 0.010, 0.015, 0.020 and 0.025, respectively) were prepared via conventional solid-state reaction process. The raw materials are zinc oxide (ZnO, > 99.0%, Sinopharm Chemical Reagent Co., Ltd, China), antimony trioxide (Sb_2O_3, > 99.0%, Sinopharm Chemical Reagent Co., Ltd, China). For each batch of experiment, the stoichiometric amounts of starting materials were weighed according to the designed composition of $Zn_{1-x}Sb_xO$ followed by ball milling for 1 h. The slurry mixtures were dried at 110 °C for one day. Then the mixture powders were calcined at 1000 °C in air for 5 h. The calcined powders were granulated with appropriate amount of polyvinyl alcohol solution (PVA) as binder, and then were pressed into pellets with a diameter of 12 mm and a thickness of about 3 mm. The green pellets were sintered in air at 1300 °C for 1 h. Both opposite sides of each as-sintered ceramic were polished and coated with silver paste followed by being heated at 600 °C for 5 min to make ohmic electrodes.

2.2 Material characterization

Phase composition of $Zn_{1-x}Sb_xO$ ceramics was determined by using X-ray diffraction (XRD, Rigaku D/max 2500, Japan) with Cu Kα radiation (λ = 0.154056 nm) with scanning rate of 8°/min. The ceramics were broken into pieces and the fracture surfaces were observed in a scanning electron microscope (SEM, JEOL 7900F). Energy dispersive X-ray spectroscopy (EDS, Oxford Ultim Max 65) attached to the SEM was employed to analyze the elemental distribution inside ceramics. Valence states were analyzed by X-ray photoelectron spectroscopy (ESCALAB 250Xi, ThermoFisher, USA).

Temperature dependence of resistance (*R*–*T*) characteristics of all ceramics were tested in range of 25 ~ 250 °C (*i.e.*, 298 ~ 523 K) by resistance temperature measurement system (ZWX-C, China) under direct current (DC) condition. Taken into account of sample size, the resistivities (ρ) of each sample were calculated according to formula $\rho = RS/h$, where *R* is the resistance of the sample, *S* and *h* are the area and thickness, respectively. The alternating current (AC) impedance spectra were measured by an electrochemical measurement system (Gamry reference600, USA) with the frequency ranging from 1 Hz to 1 MHz at different temperatures. The impedance data were analyzed by Gamry analyst program.

In order to test the aging property, samples were heat treated at 150 °C in air for 1000 h, and their room temperature resistances were measured after being aged every 100 h. The room temperature resistance was measured by a Multimeter (FLUKE, 8808A, USA), in a constant temperature room controlled by air conditioner.

3 Results and discussion

3.1 Phase component and microstructure

Figure 1 shows XRD patterns of the as-sintered ceramics of undoped ZnO, $Zn_{0.995}Sb_{0.005}O$, $Zn_{0.985}Sb_{0.015}O$ and $Zn_{0.980}Sb_{0.020}O$. Where, the upper-right inset shows the enlarged XRD patterns between diffraction angles (2θ) from 30° to 38°. The XRD patterns could be indexed to the hexagonal wurtzite structure with a space group of $P6_3mc$ (186) (cited by PDF No. 89-0511). There is no impurity phase in undoped ZnO. While, some slight peaks as marked by "filled square" in the pattern from secondary phase in $Zn_{0.985}Sb_{0.015}O$ and $Zn_{0.980}Sb_{0.020}O$ ceramics can be detected. The related peaks were analyzed to be in accordance with the one of $Zn_7Sb_2O_{12}$ phase (cited by PDF No. 74-1858).

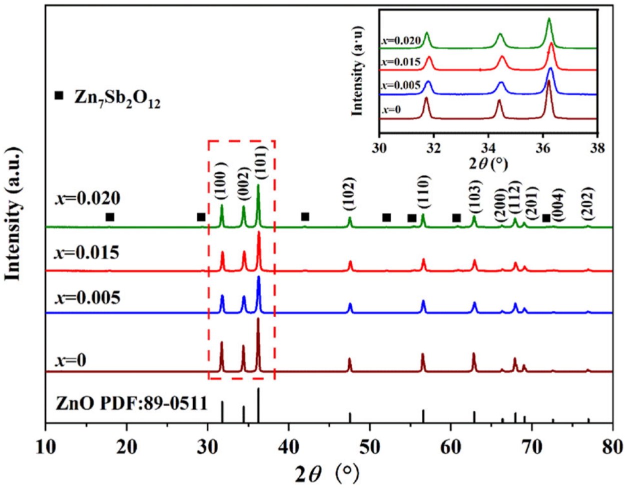

Fig. 1 XRD patterns of as-sintered $Zn_{1-x}Sb_xO$ ceramics with different contents of Sb-ions, the upper-right inset shows enlarged XRD patterns of the region marked by a dash-line rectangle

As shown in the upper-right inset in Fig. 1, XRD peaks of $Zn_{1-x}Sb_xO$ ceramics shift first to higher diffraction angles with increase of Sb-ion content till $x = 0.015$, and then shifts slightly to lower diffraction angles for $x = 0.020$. Refined by using Jade 6.0 + PDF 2004 program, the lattice parameters of the ceramics were obtained and are shown in Table 1. The lattice parameters change with the increase of Sb-ion concentration, indicating that Sb-ions have substituted into ZnO lattice.

The reason for the variation of lattice parameters depending on the Sb-ion concentration can be explained as following. Although Sb_2O_3 was selected as the raw material in this work, many studies have revealed that Sb^{3+} ion could be oxidized to be higher valence ions such as Sb^{5+} ion at elevated temperatures [21, 31–33]. As will be presented in the XPS analysis in Fig. 4, Sb^{5+} and Sb^{3+} ions co-exist in $Zn_{1-x}Sb_xO$ ceramics. The ionic radii of Sb-ions (0.060 nm for Sb^{5+} and 0.076 nm for Sb^{3+}) are difference from the one of Zn^{2+} (0.075 nm), so the substitution of Sb-ions changed the lattice parameters of $Zn_{1-x}Sb_xO$ ceramics. With low concentration of Sb-ion in $Zn_{1-x}Sb_xO$ ceramics, most of Sb^{3+} ions could be oxidized to Sb^{5+} ions (please also see in analysis in Fig. 4c). The radius of Sb^{5+} ion is smaller than that of Zn^{2+} ion, the substitution of Sb-ions into ZnO lattice resulted in a decrease in lattice parameters, and the lattice parameters decrease with the increase of Sb-ion concentration. So, according to the Bragg's law, the XRD peaks shifted towards higher diffraction angle with the increase of Sb-ion concentration. But, when the concentration of Sb-ion in $Zn_{1-x}Sb_xO$ ceramics is high enough, and because there is large difference of ionic valences between Zn^{2+} and Sb^{5+} ions, the concentration of Sb-ion may excess solid

Table 1 Lattice parameters (a and c) and cell volume (V) of $Zn_{1-x}Sb_xO$ ceramics refined from the XRD patterns as shown in Fig. 1

x in $Zn_{1-x}Sb_xO$	a (nm)	b (nm)	V ($\times 10^{-3}$ nm^3)
0	0.3253	0.5207	47.73
0.005	0.3251	0.5202	47.60
0.015	0.3250	0.5201	47.57
0.020	0.3253	0.5205	47.68

solubility of Sb-ions in ZnO lattice. Therefore, impurity or secondary phase might occur, for example, $Zn_7Sb_2O_{12}$ was detected as shown in Fig. 1. According to the research by Park et al. [31], ZnO reacted with Sb_2O_3 to form $ZnSb_2O_6$ at 700 °C and then $ZnSb_2O_6$ reacted with ZnO to form $Zn_7Sb_2O_{12}$ at 1000 °C. For the Sb-ion is Sb^{5+} in $Zn_7Sb_2O_{12}$, there might be more Sb^{3+} ions than Sb^{5+} ions substituted into ZnO lattice. Because the radius of Sb^{3+} ion is larger than that of Zn^{2+} ion, the substitution of Sb-ions into ZnO lattice should result in the increase of lattice parameters. Therefore, the XRD peaks shifted toward a lower diffraction angle when the content of Sb-ion in $Zn_{1-x}Sb_xO$ ceramics is higher, *e.g.*, the XRD peaks of $Zn_{0.980}Sb_{0.020}O$ ceramic shifted slightly toward left comparing to the ones of $Zn_{0.985}Sb_{0.015}O$ ceramic.

SEM micrographs obtained for undoped ZnO, $Zn_{0.990}Sb_{0.010}O$, $Zn_{0.985}Sb_{0.015}O$ and $Zn_{0.980}Sb_{0.020}O$ ceramics are shown in Fig. 2. The grains are closely bonded to each other although some pores exist in all samples. The measured densities (ρ_M) and porosities (P) of the ceramics were obtained by the Archimedes mothed. The relative density (ρ_r) and P of each sample can be calculated by using the relationship of $\rho_r = \rho_M/\rho_L$ and $P = (\rho_L - \rho_M)/\rho_L$, respectively, where ρ_L is theoretical density of ZnO crystal. The relative density of undoped ZnO, $Zn_{0.990}Sb_{0.010}O$, $Zn_{0.985}Sb_{0.015}O$ and $Zn_{0.980}Sb_{0.020}O$ ceramics are 83.8%, 91.82%, 92.03% and 93.23%, and the corresponding porosity is 16.2%, 8.18%, 7.97% and 6.77%, respectively. With the increase of Sb-ion content, the density increased and the porosity decreased. The existence of second phase $Zn_7Sb_2O_{12}$ might be helpful to improve the ceramic sintering-ability through formation of liquid phase [34].

The element distribution by EDS elemental mapping was performed for $Zn_{0.980}Sb_{0.020}O$ ceramic, and the results are shown in Fig. 3. Zn and O are almost evenly distributed (see in Fig. 3b, c). The EDS mapping of Sb displays some segregating regions as shown in Fig. 3d, which could be originated from the second phase $Zn_7Sb_2O_{12}$ according to the XRD analysis.

The full XPS spectra of $Zn_{1-x}Sb_xO$ ($x = 0.010$, 0.015 and 0.020) ceramics are shown in Fig. 4a. The characteristic peaks of Zn, O and Sb can be observed. Some characteristic peaks were fitted by XPS PEAK 4.1 software, and the analyzed results are shown in Fig. 4b, c. Figure 4b shows the 2*p* orbital energy spectra of Zn in $Zn_{1-x}Sb_xO$ ceramics. The binding energies (E_b) of fitted Zn 2*p* narrow spectra are shown in Table 2. The peak pairs of binding energies

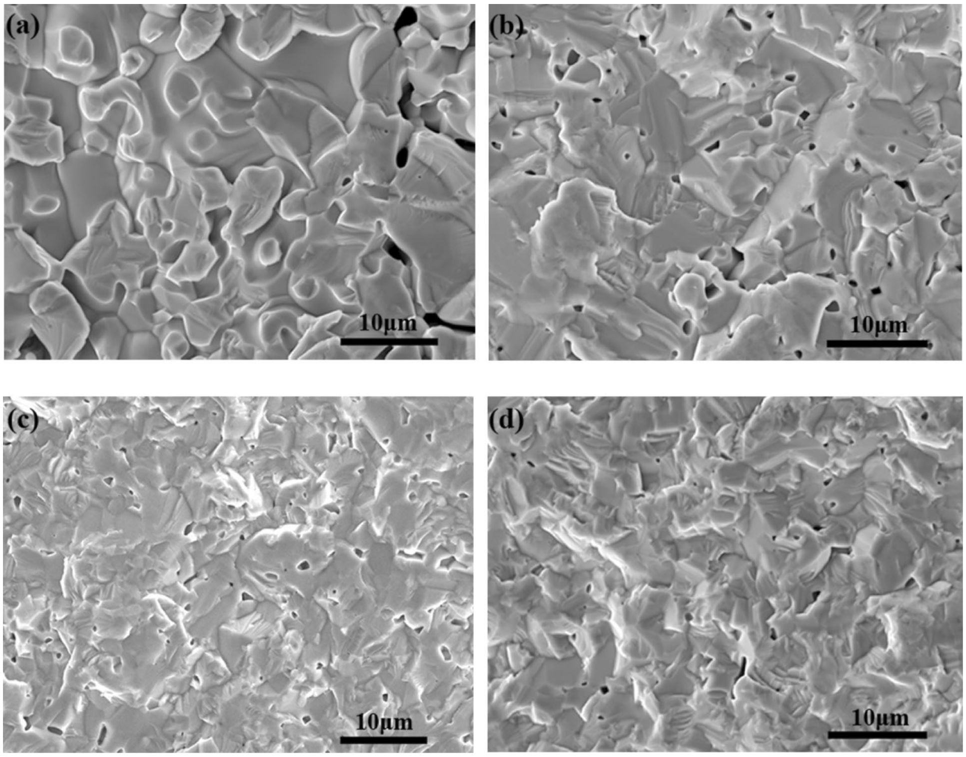

Fig. 2 SEM observations of fracture surface of $Zn_{1-x}Sb_xO$ ceramics, **a** $x = 0$, **b** $x = 0.005$, **c** $x = 0.010$, **d** $x = 0.020$

Fig. 3 EDS elemental mapping analysis of $Zn_{0.980}Sb_{0.020}O$ ceramic, **a** SEM image, **b** Zn distribution mapping, **c** O distribution mapping, **d** Sb distribution mapping

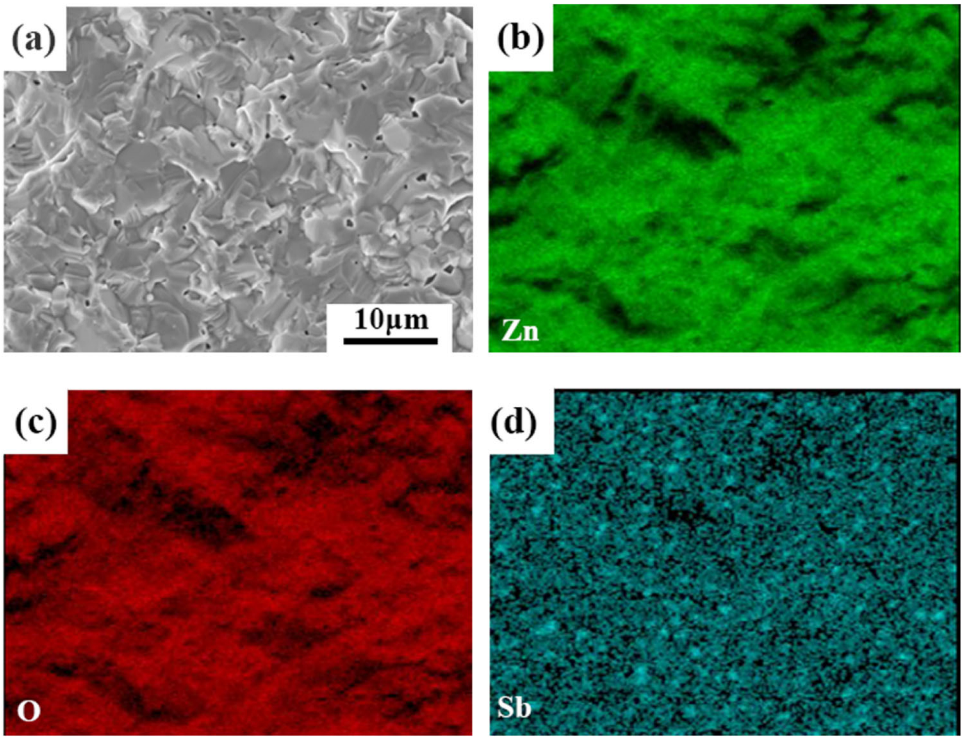

Fig. 4 Analysis of XPS spectra of $Zn_{1-x}Sb_xO$ (x = 0.010, 0.015 and 0.020) ceramics, **a** full spectra, **b** Zn 2p narrow spectra, **c** Sb 3d narrow spectra

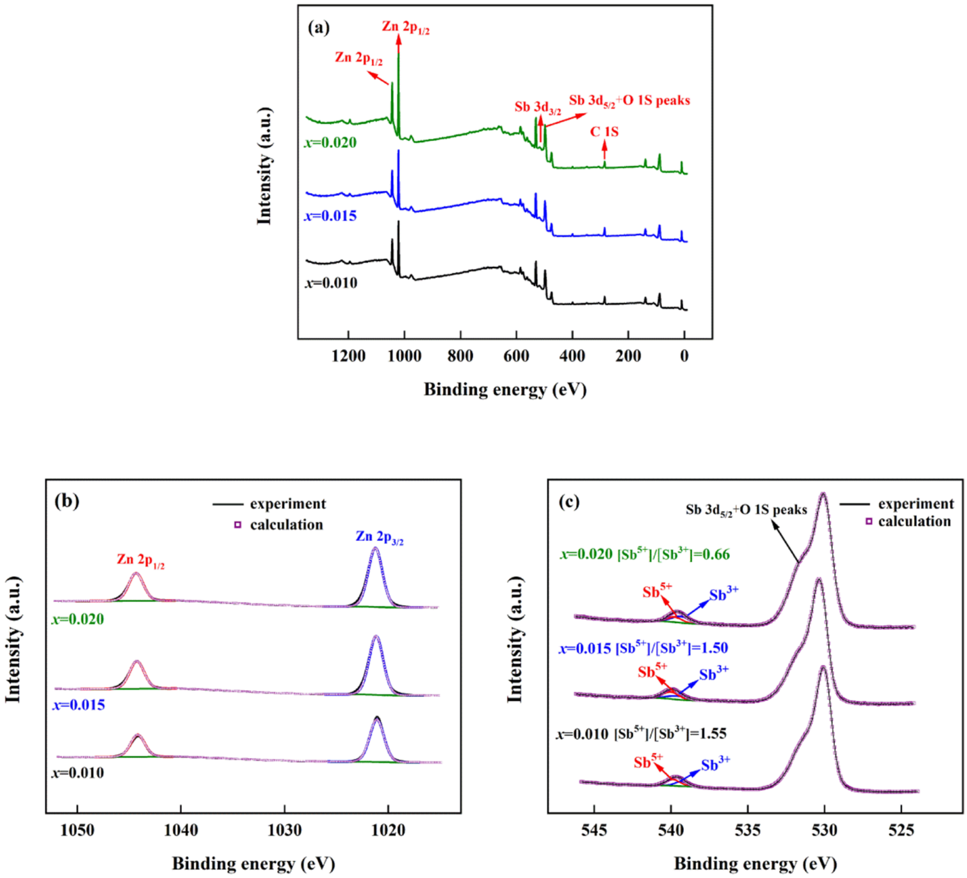

at about 1021 eV and 1044 eV correspond to $2p_{3/2}$ and $2p_{1/2}$, respectively [18], indicating that Zn^{2+} ions exist in $Zn_{1-x}Sb_xO$ (x = 0.010, 0.015 and 0.020) ceramics.

Considering that the binding energies of O 1*s* and Sb $3d_{5/2}$ are superimposed, only the Sb $3d_{3/2}$ is reported [35]. As shown in Fig. 4c, each Sb $3d_{3/2}$ narrow spectrum consists of two peaks of about 540 eV and 539 eV. The binding energies (E_b) of fitted Sb $3d_{3/2}$ narrow spectra are shown in Table 2. The two peaks are contributed by Sb^{5+} and Sb^{3+} ions, respectively [35, 36]. These indicate that Sb-element in $Zn_{1-x}Sb_xO$ ceramics has two kinds of valence states, *i.e.*, Sb^{5+} and Sb^{3+}. Compared with the areas of two fitted peaks, the ratios of Sb^{5+} and Sb^{3+} ionic contents $[(Sb^{5+})/(Sb^{3+})]$ were calculated to be 1.55/1 for $Zn_{0.990}Sb_{0.010}O$, 1.50/1 for $Zn_{0.985}Sb_{0.015}O$ and 0.66/1 for $Zn_{0.980}Sb_{0.020}O$ respectively. These indicate that Sb^{5+} is the dominant valence state of Sb element in $Zn_{0.990}Sb_{0.010}O$ and $Zn_{0.985}Sb_{0.015}O$ ceramic, while the Sb element in $Zn_{0.980}Sb_{0.020}O$ ceramic is dominated by Sb^{3+}.

3.2 Electrical properties

Figure 5a, b show the plots of relationship between logarithm of resistivity (lnρ) and reciprocal of absolute temperature (1000/T) of $Zn_{1-x}Sb_xO$ ceramics for various contents of Sb-ion. The ρ_{25} values of ceramics with various contents of Sb-ion are shown in Table 3. When $x \leq 0.005$, ρ_{25} decreased with the increase of Sb-ion content (see in Fig. 5a). While, ρ_{25} increased with the increase of Sb-ion content when $x \geq 0.005$ (see in Fig. 5b). ρ_{25} of undoped ZnO and $Zn_{0.995}Sb_{0.005}O$ ceramics are 662 kΩ cm and 57.18 kΩ cm, respectively. The decrease of ρ_{25} for the introduction of Sb-ions should result from the doping effect of semiconductor, and the related defect reaction can be shown in Eqs. (1) and (2).

$$Sb_2O_5 \xrightarrow{ZnO} 2Sb_{Zn}^{\cdots} + 2O_O + \frac{3}{2}O_2 + 6e' \quad (1)$$

$$Sb_2O_3 \xrightarrow{ZnO} 2Sb_{Zn}^{\cdot} + 2O_O + \frac{1}{2}O_2 + 2e' \quad (2)$$

Here, Sb_2O_3 and Sb_2O_5 act as donor for ZnO semiconductor. The weak binding electrons introduced by Sb-ion doping locate in the donor level, and can be easily thermally activated to the conduction band, and enhanced conductivity of ZnO based ceramics.

However, the ρ_{25} increased with the increase of Sb-ion content when $x \geq 0.005$ (see in Fig. 5b). As shown in Eqs. (1) and (2), the concentration of electrons increased in proportion to the content of Sb-ion in the $Zn_{1-x}Sb_xO$ ceramics, but one could not conclude that the conductivity of the ceramics must increase monotonously with the increase of Sb-ion content. Because any semiconductor material has an appropriate doping concentration, at which the semiconductor material has highest conductivity and minimal ρ_{25}. When the Sb-ion content is higher than an appropriate quantity, accumulation and aggregation of the produced electrons may take place, resulting in the increase of ρ_{25}. On the other hand, the solid solubility of Sb-ion in ZnO crystal is limited, the excess Sb-ions might locate at grain boundaries in the status of antimony oxides such as Sb_2O_3 and Sb_2O_5, and might react with ZnO to form $Zn_7Sb_2O_{12}$ second phase. The second phase normally locates at the grain boundaries, increases the barrier of grain boundary and hinders the transportation of electrons. So the grain boundary resistance of ceramics increased, and the total resistivity of ceramics increased.

All of the $Zn_{1-x}Sb_xO$ ceramics show typical NTC characteristics with good linear relationship of lnρ-1000/T in the test temperature range excepting for the undoped ZnO and $Zn_{0.999}Sb_{0.001}O$ ceramics. The linear relationship of $\ln\rho - 1000/T$ plots can be described by the Arrhenius law as shown in Eq. (3).

$$\rho_T = \rho_0 \exp\left(\frac{E_a}{kT}\right) = \rho_0 \exp\left(\frac{B}{T}\right), \quad (3)$$

where, ρ_T is resistivity at temperature T (in Kelvin), ρ_0 is a constant related to material characteristic, k is the Boltzmann constant, E_a is activation energy of conduction, B is a parameter reflecting the temperature sensitivity of a NTC thermistor and has a unit in Kelvin (K).

Table 2 Fitted E_b (eV) at the peaks of XPS narrow spectra in $Zn_{1-x}Sb_xO$ (x = 0.010, 0.015 and 0.020) ceramics

x in $Zn_{1-x}Sb_xO$	E_b (Zn $2p_{1/2}$)	E_b (Zn $2p_{3/2}$)	E_b (Sb $3d_{3/2}$, Sb^{5+})	E_b (Sb $3d_{3/2}$, Sb^{3+})
0.010	1044.17	1021.10	540.18	539.62
0.015	1044.25	1021.17	540.03	539.49
0.020	1044.33	1021.25	539.76	539.22

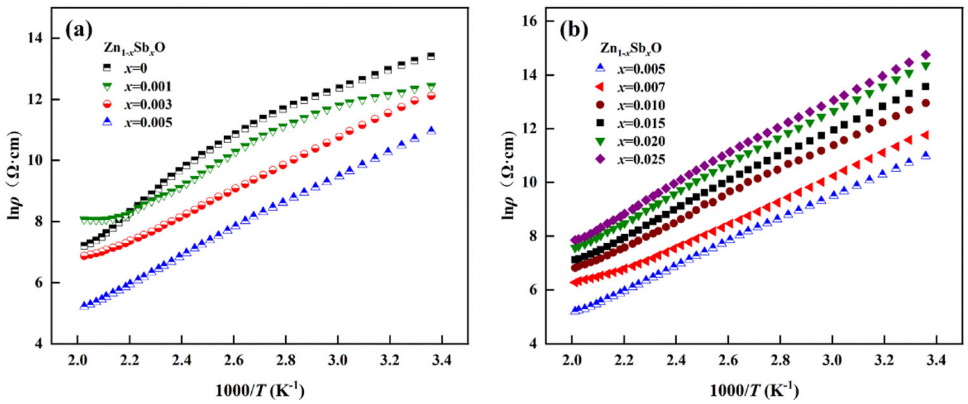

Fig. 5 Electrical properties of $Zn_{1-x}Sb_xO$ ceramics with various contents of Sb-ions, **a** temperature dependence of resistivity for $0 \le x \le 0.005$, **b** temperature dependence of resistivity for $0.005 < x \le 0.02$

Table 3 Resistivity (ρ_{25}), $B_{25/85}$ value, E_a and TCR_{25} of the $Zn_{1-x}Sb_xO$ ceramics

x in $Zn_{1-x}Sb_xO$	ρ_{25} (kΩ·cm)	$B_{25/85}$ (K)	E_a (eV)	TCR_{25} (% K^{-1})
0	662	3014	0.260	− 3.39
0.001	253.37	2284	0.197	− 2.57
0.003	245.73	3961	0.341	− 4.62
0.005	57.18	4103	0.354	− 4.62
0.007	127.74	4273	0.368	− 4.81
0.010	225.21	4382	0.378	− 4.93
0.015	451.13	4536	0.391	− 5.11
0.020	821.51	4754	0.410	− 5.35
0.025	2591.50	4744	0.409	− 5.34

The B value and temperature coefficient of resistance (TCR) are usually used to characterize the temperature sensitivity of NTC thermistor. The B value and TCR_{25} value can be calculated by Eqs. (4) and (5), respectively.

$$B = \frac{\ln\rho_1 - \ln\rho_2}{1/T_1 - 1/T_2} \tag{4}$$

$$\mathrm{TCR}_{25} = -\frac{E_a}{kT_{25}^2} = -\frac{B_{25}}{T_{25}^2} \tag{5}$$

where, ρ_1 and ρ_2 are resistivities at temperatures of T_1 and T_2, respectively. T_1 and T_2 are often chosen as 298 K (25 °C) and 358 K (85 °C), respectively. So the B value is usually written as $B_{25/85}$. The relevant $B_{25/85}$, E_a and TCR_{25} values of ZnO based ceramics with different Sb-ion concentrations are listed in Table 3. The high $B_{25/85}$ values (2284 K ~ 4754 K) and TCR_{25} (− 2.57% ~ − 5.35%/K) indicate that $Zn_{1-x}Sb_xO$ ceramics are high temperature sensitivity. With the increase of Sb-ion content, $B_{25/85}$ values show increasing trend. The high $B_{25/85}$ and adjustable ρ_{25} enhance the potential application of $Zn_{1-x}Sb_xO$ ceramics for NTC thermistors.

3.3 Impedance spectrum analysis

The electrical properties of ceramics are generally contributed from grain effect, grain boundary effect and electrode polarization effect. Analysis of complex impedance spectroscopy (CIS) is an effective way to characterize the electrical properties of ceramics [12–14, 18–21]. Here, CISs in Nyquist plots of $Zn_{1-x}Sb_xO$ ceramics were measured at room temperature and analyzed as shown in Fig. 6. Each plot looks containing one arc. In order to reveal the characteristic of the CISs, an equivalent circuit as the inset in Fig. 6a was selected to fit the CISs. Where, R_g and R_{gb} respectively represent the resistances from grain effect and grain boundary effect, R_0 is a resistance coming from the measurement system, CPE_g and CPE_{gb} are the related constant phase elements which is caused by internal inhomogeneity or defects for grain effect and grain boundary effect, respectively. One can see that the equivalent circuit fitted the Nyquist plots well. The fitted results are shown in Table 3. This indicates that each CIS is composed of both grain effect and grain boundary effect.

It can be seen from Table 4 that, for the undoped ZnO ceramic, R_g is much higher than R_{gb}. After

Fig. 6 Analysis of complex impedance spectra in Nyquist plots of $Zn_{1-x}Sb_xO$ ceramics measured at room temperature, **a** $x = 0$, **b** $x = 0.005$, 0.007, 0.010, 0.015, **c** $x = 0.020$, 0.025

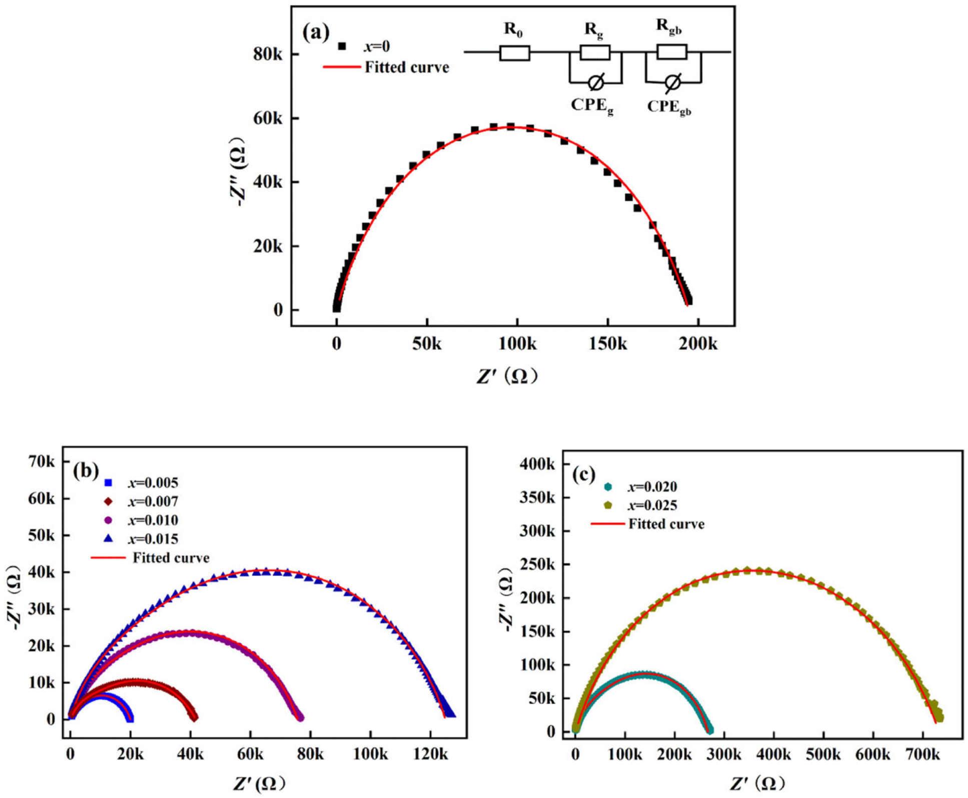

doping with Sb-ions, R_g of each sample decreased and always less than the related R_{gb}. When x is 0.005, the $Zn_{1-x}Sb_xO$ ceramic has a minimum R_g of 3.03 kΩ which is much lower than R_g of undoped ZnO ceramic. While, R_{gb} is higher than the related R_g in each Sb–doped ZnO ceramic. Both R_g and R_{gb} increase with the increase of Sb-ion content in the Sb-doped ZnO ceramics when x is larger than 0.005. As shown in Eqs. (1) and (2), substitution of Sb-ions in ZnO lattice resulted in the occurrence of electronic charge carriers, and enhances the conductivity of ZnO semiconductor. While, as discussed in Figs. 1 and 3, the solid solubility of Sb-ion in ZnO lattice should be very small, excessive Sb-ions and the produced secondary phase of $Zn_7Sb_2O_{12}$ might locate at grain boundaries, resulting in the increase of grain boundary resistance.

Table 4 Fitted results of Nyquist plots of $Zn_{1-x}Sb_xO$ ceramics by using the equivalent circuit as the inset in Fig. 5a, grain resistance (R_g), grain boundary resistance (R_{gb}) and total resistance ($R_g + R_{gb}$)

x in $Zn_{1-x}Sb_xO$	R_g (kΩ)	R_{gb} (kΩ)	$R_g + R_{gb}$ (kΩ)
0	187.72	7.15	194.87
0.005	3.03	16.93	19.96
0.007	5.64	36.06	41.70
0.010	9.45	66.18	75.63
0.015	13.42	112.50	125.92
0.020	41.60	225.10	266.70
0.025	149.70	582.50	732.20

3.4 Electrical stability

The practical applications of NTC thermistors need high electrical stability. In order to investigate the electrical stability of the studied ceramics, two kinds of test ways were conducted in this work: one is repeated measurement of temperature dependence of resistivity of $Zn_{0.990}Sb_{0.010}O$ and $Zn_{0.985}Sb_{0.015}O$ ceramics, another is to gauge the resistance shift of the ceramics during 150 °C aging treatment.

Figure 7a shows the plots of temperature dependence of resistivity ($\ln\rho - 1000/T$ plots) that were repeatedly tested for 7 times in temperature range between 25 and 250 °C (*i.e.*, 298 ~ 548 K) of a $Zn_{0.990}Sb_{0.010}O$ ceramic. Figure 7b shows the 7-times repeatedly tested $\ln\rho - 1000/T$ plots of a $Zn_{0.985}Sb_{0.015}O$ ceramic. Both of the repeatedly tested plots show that the ceramics have high repeatability of R–T characterization.

In the meanwhile, $Zn_{1-x}Sb_xO$ ceramics with Ag electrodes have also been aged at 150 °C in air. Figure 8a shows the related resistance change rates ($\Delta R/R_0$) after being aged for different periods. After having been aged for 1000 h, the $\Delta R/R_0$ are 1.44%, 1.77%, 1.98%, 2.09%, 2.17% for $Zn_{0.995}Sb_{0.005}O$, $Zn_{0.990}Sb_{0.010}O$, $Zn_{0.985}Sb_{0.015}O$, $Zn_{0.980}Sb_{0.020}O$ and $Zn_{0.975}Sb_{0.025}O$ ceramics, respectively. These indicate that the Sb–doped ZnO NTC ceramics have good electrical stability.

To further investigate the aging characteristics, the CISs of $Zn_{0.990}Sb_{0.010}O$ and $Zn_{0.985}Sb_{0.015}O$ ceramics before and after aging treatment were also analyzed and are shown in Fig. 8b. Each sample has similar Nyquist plots before and after aging treatment. The Nyquist plots were fitted with the equivalent circuit as the inset in Fig. 6a. For $Zn_{0.990}Sb_{0.010}O$ ceramic, R_g, R_{gb} and $R_g + R_{gb}$ are 9.87 kΩ, 66.85 kΩ and 76.72 kΩ after aging, and the related resistance change rates are 8.87%, 1.01% and 1.44%, respectively, compared with those before aging. For $Zn_{0.985}Sb_{0.015}O$ ceramic, R_g, R_{gb} and $R_g + R_{gb}$ are 14.35 kΩ, 113.80 kΩ and 128.15 kΩ after aging, and the related resistance change rates are 6.93%, 1.16% and 1.77%, respectively, compared with those before aging. These indicate that the total resistance change rates of the tested samples are consistent with the results of aging test as shown in Fig. 8a, and the aging induced resistance change mainly comes from the grain effect (R_g).

Figure 9a shows XPS spectra of $Zn_{0.990}Sb_{0.010}O$ ceramic before and after aging. Both XPS spectra have not obvious difference in binding energy peaks. The narrow spectra of Sb $3d_{3/2}$ are fitted by XPS PEAK 4.1 software and shown in Fig. 9b. The results show that the Sb $3d_{3/2}$ narrow spectrum before aging is composed of two peaks with binding energies of 540.18 eV and 539.62 eV, corresponding to Sb^{5+} and Sb^{3+} ions, respectively. The Sb $3d_{3/2}$ narrow spectrum of the aged sample can be fitted to consist with two peaks of 540.29 eV and 539.74 eV, corresponding to Sb^{5+} and Sb^{3+} ions, respectively. These indicate that the ionic species of the ceramics did not change before and after aging. According to the fitted peaks, the ratio of $[Sb^{5+}]/[Sb^{3+}]$ cationic contents in the aged $Zn_{0.990}Sb_{0.010}O$ ceramic is 1.52/1, which is slightly less than that before aging (1.55/1).

As discussed in Figs. 5 and 6 for the conductivity characteristics, and mentioned in Eqs. (1) and (2), the conductivity of Sb–doped ZnO ceramics is affected by the contents and valent states of Sb-ions. The valence change of Sb-ions induced by aging might result from the change of electron numbers in ceramics, for example, capturing or losing electrons from the adsorbed gas on the ceramic surface. While, the increases of electron carriers induced by Sb-ion doping are due to the introduction of higher valence ions (Sb^{5+} and Sb^{3+} ions) into ZnO–based ceramics, as shown in Eqs. (1) and (2). The aging treatment was performed in air, and it is possible that the moisture (water) and oxygen are adsorbed on the ceramic surface. During aging, it is possible that the electrons at the valence band can be thermally activated into conduction band, and electron holes ($\dot{h}$) were left at valence band. For the suitable conduction band and valence band positions of Sb–doped ZnO, the redox reactions of the adsorbed water (H_2O_{ads} or $OH^-{}_{ads}$) as following equations form reactive species of $HO\cdot$ for that the reaction energy of is 2.38 eV *vs*. the normal hydrogen electrode (NHE) [29, 37, 38]. These reactions consume the holes in the valence band.

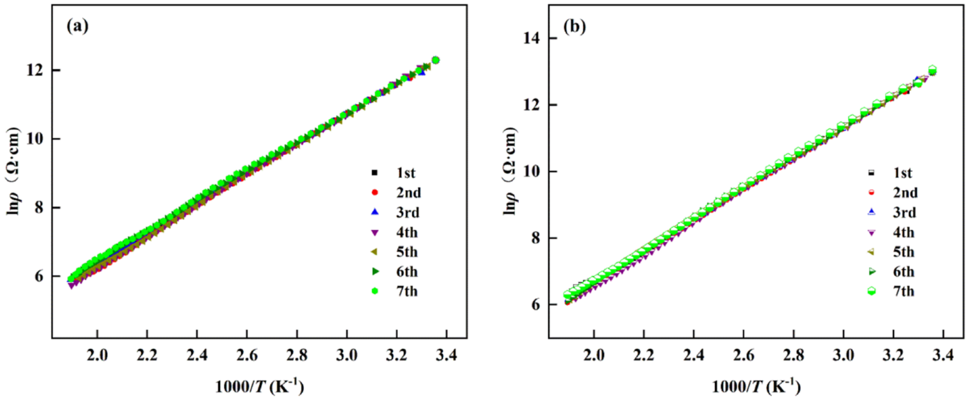

Fig. 7 lnρ − 1000/T plots of $Zn_{1-x}Sb_xO$ ceramics repeatedly measured for seven times in temperature range between 25 and 250 °C, **a** $x = 0.010$, **b** $x = 0.015$

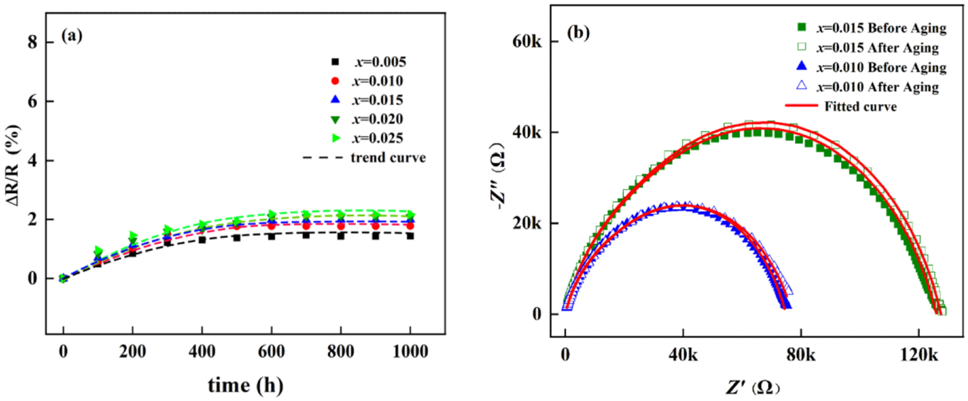

Fig. 8 Aging characteristic of $Zn_{1-x}Sb_xO$ ceramics, **a** resistance shift rates ($\Delta R/R_0$) of $Zn_{1-x}Sb_xO$ ceramics aged at 150 °C for different time, $x = 0.005 \sim 0.025$, **b** room temperature Nyquist plots of $Zn_{0.990}Sb_{0.010}O$ and $Zn_{0.985}Sb_{0.015}O$ ceramics before and after aging

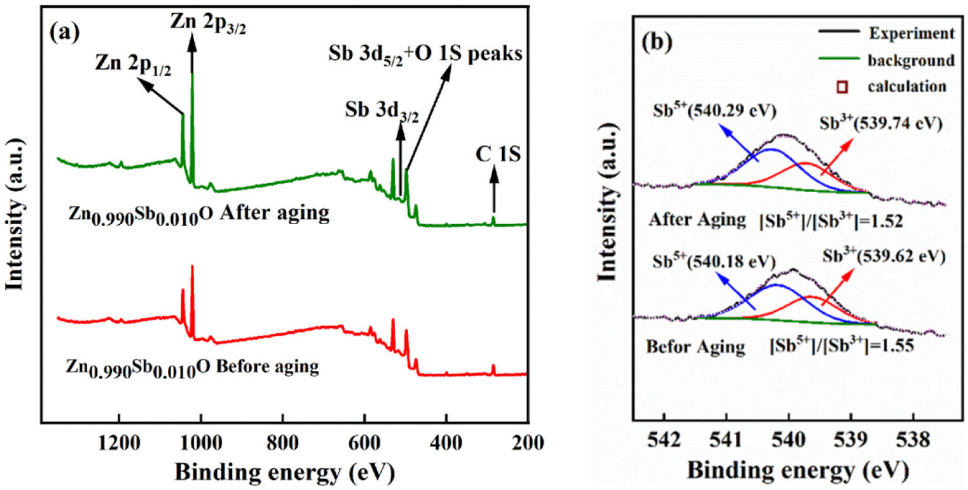

Fig. 9 XPS spectra of the $Zn_{0.990}Sb_{0.010}O$ ceramic before and after aging, **a** full spectra, **b** Sb $3d_{3/2}$ narrow spectra

$$h^{\cdot} + H_2O_{ads} \rightarrow HO\cdot + H^+ \tag{6}$$

$$h^{\cdot} + H_2O_{ads} \rightarrow \frac{1}{2}O_2 + 2H^+ \tag{7}$$

$$h^{\cdot} + OH^-_{ads} \rightarrow HO\cdot \tag{8}$$

On the other hand, the electrons that were thermally activated from valence band into conduction band might transfer to ceramic surface, return to valence band and be trapped by cations such as Sb^{5+} ions. When the electrons were trapped by Sb^{5+} ions, the Sb^{5+} ions might be reduced to be Sb^{3+} ions, leading to the decrease of quantity of Sb^{5+} ions. So the quantity of electrons occurred by Eq. (1) became less, and the whole content of charge carriers in the ceramics reduced, leading to the increase of their resistivity.

The $[Sb^{5+}]/[Sb^{3+}]$ ratio has little change comparing the ones before aging with that after aging, indicating the aging process of $Zn_{0.990}Sb_{0.010}O$ ceramics has little effect on the valence states of Sb-ions. The analysis in Fig. 9 reveals that the Sb-ions have good valent stability, resulting in high electrical stability during ageing process. For the simple chemical composition, adjustable resistivity and temperature sensitivity, the Sb–doped ZnO ceramics should have good potential for application as NTC thermistors.

4 Conclusions

Sb–doped ZnO ($Zn_{1-x}Sb_xO$, $x \leq 0.025$) ceramics have the hexagonal wurtzite structure and exhibit typical NTC effect. The ceramic resistivity is composed of both grain effect and grain boundary effect. The $Zn_{1-x}Sb_xO$ NTC ceramics have high temperature sensitivity with $B_{25/85}$ values from 2284 to 4744 K, and their room temperature resistivity can be effectively adjusted from 57.18 to 2591.5 kΩ·cm by changing the concentration Sb-ions. The studied NTC ceramics show high electrical stability with resistance change rates ranging from 1.44 to 2.17% after aging treatment at 150 °C in air for 1000 h. For the simple chemical composition, adjustable resistivity and temperature sensitivity, the Sb–doped ZnO ceramics should have good potential for application as NTC thermistors.

Acknowledgements

This work is supported by the research funds from the National Natural Science Foundation of China (Grant No. 51767021), Research and development program in key areas of Guangdong Province (Grant No. 2019B090913002), Research and development project of Hunan Wedid Materials Technology Co., Ltd., China (Grant No. 738010241), and the general project of scientific research project of Hunan Provincial Department of Education Scientific (Grant No. 19C0342).

Declarations

Conflict of interest The authors declare that they have no known competing financial interests or personal relationships that could have appeared to influence the work reported in this paper.

References

1. M. Schubert, C. Münch, S. Schuurman, V. Poulain, J. Kita, R. Moos, J. Eur. Ceram. Soc. **38**, 613–619 (2018)
2. H. Gao, C.J. Ma, B. Sun, J. Mater. Sci. Mater. Electron. **25**, 3990–3995 (2014)
3. J. Wang, H. Zhang, X. Sun, Y. Liu, Z. Li, J. Mater. Sci. Mater. Electron. **27**, 11902–11908 (2016)
4. M. Schubert, C. Münch, S. Schuurman, V. Poulain, R. Moos, J. Eur. Ceram. Soc. **38**, 613–619 (2018)
5. A. Feteira, J. Am. Ceram. Soc. **92**, 967–983 (2009)
6. C.J. Ma, H. Gao, J. Alloys Compd. **749**, 853–858 (2018)
7. C.J. Ma, H. Gao, J. Mater. Sci. Mater. Electron. **28**, 6609–6703 (2017)
8. K. Park, Mater. Sci. Eng. B **104**, 9–14 (2003)
9. J.M. Varghese, A. Seema, K.R. Dayas, Mater. Sci. Eng. B **149**, 47–52 (2008)
10. E.D. Macklen, J. Phys. Chem. Solids. **47**, 1073–1079 (1986)
11. J. Jung, J. Töpfer, J. Mürbe, A. Feltz, J. Eur. Ceram. Soc. **6**, 351–369 (1990)
12. Z. Yang, H. Zhang, Z. He, B.C. Li, Z. Li, J. Mater. Sci. Mater. Electron. **30**, 3088–3097 (2019)
13. X. Sun, Z. Li, W. Fu, S. Chen, H. Zhang, J. Mater. Sci. Mater. Electron. **29**, 343–350 (2017)
14. Y. Zeng, Z. Li, J. Shao, X. Wang, H. Zhang, J. Mater. Sci. Mater. Electron. **30**, 14528–14537 (2019)
15. H. Zhang, T. Liu, L. Zhao, H. Jiang, A. Chang, J. Mater. Sci. Mater. Electron. **28**, 14195–14201 (2017)
16. M. Chen, H. Zhang, T. Liu, H. Jiang, A. Chang, J. Mater. Sci. Mater. Electron. **28**, 18873–18878 (2017)
17. J. Wang, H. Zhang, D. Xue, Z. Li, J. Phys. D **42**, 235103 (2009)
18. B. Yang, H. Zhang, J. Zhang, X. Zhang, Z. Li, J. Mater. Sci. Mater. Electron. **26**, 10151–10158 (2015)
19. J. Wang, H. Zhang, X. Sun, Y. Liu, Z. Li, J. Mater. Sci. Mater. Electron. **27**, 1–7 (2016)
20. P. Li, H. Zhang, C. Gao, G. Jiang, Z. Li, J. Mater. Sci. Mater. Electron. **30**, 19598–19608 (2019)
21. P. Ouyang, H. Zhang, Y. Zhang, J. Wang, Z. Li, J. Mater. Sci. Mater. Electron. **26**, 6163–6169 (2015)
22. H. Li, I. Thayil, X. Ma, X. Sang, H. Zhang, A. Chang, Ceram. Int. **46**, 24365–24370 (2020)
23. D. Fang, C. Zheng, C. Chen, A.J.A. Winnubst, J. Electroceram. **22**, 421–427 (2009)
24. F. Guan, Z.W. Dang, S.F. Huang, J.R. Wang, Y.Q. Wu, J. Eur. Ceram. Soc. **40**, 5597–5601 (2020)
25. C. Gao, Z. Li, L. Yang, D. Peng, H. Zhang, J. Eur. Ceram. Soc. **41**, 4160–4166 (2021)
26. H. Zeng, G. Duan, Y. Li, S. Yang, X. Xu, Adv. Funct. Mater. **20**, 561–572 (2010)
27. Z. Wang, J. Song, Science **312**, 242–246 (2006)
28. A. Janotti, C.G. Van de Walle, Rep. Prog. Phys. **72**, 126501 (2009)
29. Y. Wang, R. Shi, J. Lin, Y. Zhu, Energy Environ. Sci. **4**, 2922–2929 (2011)
30. S.C. Pillai, J.M. Kelly, R. Ramesh, D.E. Mccormack, J. Mater. Chem. C **1**, 3268–3281 (2013)
31. K. Park, J.K. Seong, S. Nahm, J. Alloys Compd. **455**, 331–335 (2008)
32. I. Saadeddin, H.S. Hilal, B. Pecquenard, J. Marcus, A. Mansouri, C. Labrugere, M.A. Subramanian, G. Campet, Solid State Sci. **8**, 7–13 (2006)
33. M.I. Miranda-López, V.S. Rico, M.B. Hernández, L. Falcon-Franco, S. García-Villarreal, P. Zambrano-Robledo, M. Esneider-Alcalá, L. García-Ortiz, J.A. Aguilar-Martínez, Ceram. Int. **47**, 163–172 (2021)
34. S. Ezhilvalavan, T.R.N. Kutty, Appl. Phys. Lett. **68**, 2693–2695 (1996)
35. A. Barbaro, S. Larrondo, S. Duhalde, N. Amadeo, Appl. Cata. Gen. **193**, 277–283 (2000)
36. W. Hao, H. Wu, P. Xu, Y. Shi, S. Yang, M. Wang, L. Sun, E. Gao, Y. Zhang, Ceram. Int. **43**, 3631–3638 (2017)

37. J. Chen, Z.S. Chen, X.Y. Zhang, X.F. Li, L.H. Yu, D.Z. Li, Appl. Catal. B. **210**, 379–385 (2017)
38. T. Zhu, M.N. Chong, E.S. Chan, Chemsuschem **7**, 2974–2997 (2014)